energies

MDPI

Article

Simulation and Experiments on Optimization of Vortex-Induced Vibration Power Generation System Based on Side-by-Side Double Blunt Bodies

Liguo Fan [1,2,†], Guoqiang Liu [1,3], Xianjin Song [2], Ce Xiang [1], Jiacheng Wei [2] and Hui Xia [1,3,*,†]

[1] Institute of Electrical Engineering, Chinese Academy of Sciences, Beijing 100190, China; flg354@mail.iee.ac.cn (L.F.); liuguoqiang@mail.iee.ac.cn (G.L.); xiangce@mail.iee.ac.cn (C.X.)
[2] School of Electric Power and Architecture, Shanxi University, Taiyuan 030006, China; sxsxj@163.com (X.S.); w13734007089@mail.iee.ac.cn (J.W.)
[3] University of Chinese Academy of Sciences, Beijing 100049, China
* Correspondence: xiahui@mail.iee.ac.cn
† These authors contributed equally to this work.

Abstract: In order to improve the utilization efficiency of converting low-flow current energy into electric energy for Reynolds number 10,000 ≤ Re ≤ 40,000, this paper proposes a vortex-induced vibration power generation system based on a side-by-side double blunt body. In this system, the side-by-side double blunt body structure is used in the current energy capture part to enhance the collection of low-flow current energy; the permanent magnet linear motor is used in the electric energy conversion part to improve the efficiency of electric energy conversion; and a laboratory device is constructed for testing. The effects of the blunt body structure parameters and the center spacing ratio on the energy harvesting performance of the system are qualitatively explained by constructing a simulation model. Compared with the single blunt body energy capture structure, the side-by-side double blunt body structure increases the vibration amplitude by 1.04 times and the lift by 1.14 times at the center spacing S/D = 2.4. Meanwhile, energy harvesting can be realized at a lower flow velocity, increasing the vortex-induced vibration's energy capture range. Finally, the power generation system was experimentally verified in the laboratory, and the results showed that the vibration amplitude of the double blunt body structure was increased by 1.12 times compared to the single blunt body. The maximum output power of the generator is 10.55 W when the water velocity is 0.7 m/s. The energy conversion efficiency of the power generation system can reach a maximum of 52.93%, which is 12.33% higher than that of a single blunt body structure, which proves that the system has a higher power conversion efficiency than that of a conventional single conversion system.

Keywords: low-velocity ocean current energy; vortex-induced vibration; energy conversion system; side-by-side arrangement; flexible cylinders; permanent magnet linear motors

check for updates

Citation: Fan, L.; Liu, G.; Song, X.; Xiang, C.; Wei, J.; Xia, H. Simulation and Experiments on Optimization of Vortex-Induced Vibration Power Generation System Based on Side-by-Side Double Blunt Bodies. *Energies* **2024**, *17*, 5291. https://doi.org/10.3390/en17215291

Academic Editor: Antonio T. Alexandridis

Received: 6 September 2024
Revised: 26 September 2024
Accepted: 21 October 2024
Published: 24 October 2024

Copyright: © 2024 by the authors. Licensee MDPI, Basel, Switzerland. This article is an open access article distributed under the terms and conditions of the Creative Commons Attribution (CC BY) license (https://creativecommons.org/licenses/by/4.0/).

1. Introduction

The environmental pollution problems from conventional fossil energy sources are receiving significant attention. Many scholars have actively explored renewable and clean energy sources to achieve low carbon emissions and sustainable economic development [1,2]. Marine current energy has a vast energy content and great potential for power generation. Researchers worldwide have developed many different converters to utilize ocean current energy [3,4].

When a fluid flows through a non-streamlined body (called a blunt body), the alternately shedding vortices formed downstream of it generate a cyclical lift force acting on the blunt body, causing the elastically mounted blunt body to undergo a periodic vibration, which further modifies the formation and shedding of vortices [5]. This interaction between

the fluid and the structure is called vortex-induced vibration (VIV), which is a nonlinear, wide-range, fluid-in-motion (FIM) phenomenon with multiple degrees of freedom [6]. Since the vortex-induced vibration phenomenon contains a large amount of vibrational energy, it can capture hydrokinetic energy from lower-velocity currents and convert it into mechanical and electrical energy.

Bernitsas' team [7–9] at the University of Michigan utilizes the principle of the high-amplitude response of this converter when it is started at a low flow velocity to convert the current energy into vibration mechanical energy and generate electricity. In comparison to conventional paddle-type power generation devices, the starting flow velocity of the vortex-induced vibration power generation device is less than 1 m/s, which significantly enhances the utilization of low-speed currents. Furthermore, the energy density of the single-vibrator vortex-induced vibration (VIV) power generation device is as high as 0.0691 KW/m^3, considerably higher than that of other clean energy power generation devices. The team investigated the relationship between the power and efficiency of vortex-induced vibration power generation with a cylindrical blunt body, as illustrated by the following equation, based on the VIVACE system they had developed [10].

$$P = 8\pi^3(m_b + m_a)\xi(Af)^2 f_n \quad (1)$$

where P represents power generation; m_b is the mass of the blunt body; m_a is the additional mass; A is the vibration amplitude; f is the vibration frequency; and f_n is the intrinsic frequency. It is learned that the power generation depends on the product of the amplitude and frequency of the blunt body, and for vortex-induced vibration power generation equipment, the larger the vibrator amplitude and the higher the frequency, the more conducive to the energy utilization of the power generation device system.

Current vortex-induced vibration power generation systems usually use a single cylindrical passivated body structure combined with a rotary generator or piezoelectric materials. Some scholars have investigated the use of piezoelectric materials to convert the energy captured by vortex-induced vibration into electricity. All of them have a maximum output power of mW, and the efficiency of the energy conversion is also low [11–14]. Zhang et al. [15] conducted power generation experiments using a single passivated body structure and a rotating motor, which received a large damping, with a maximum output power of 1.37 W and a conversion efficiency of 29%. Wang et al. [16] used two asymmetric manifolds to improve the capture efficiency of a vortex-excited piezoelectric energy harvester. The maximum enhancement ratio of VIVPEH's output power over the conventional VIVPEH can reach 471.2% when the angles of the two plates are 60° and 90°, respectively. Li et al. [17] used vortex-induced vibration friction electric nanogenerators to improve energy harvesting efficiency in low-speed water, with a maximum power output of 2.5 mW. Heragy et al. [18] developed a vibrational energy harvester using a magnetostrictive material as a generator and prisms as traps. The maximum power generation using a v-shaped prism as a blunt body was 5.02 mW. However, single blunt body vortex-induced vibration structures have limitations such as low amplitude and frequency, a narrow range of captured energy, and poor adaptation to currents with changing flow velocities. Piezoelectric materials can only generate milliwatts of electrical energy due to their limited energy conversion rate. This paper proposes a double blunt body structure placed side-by-side to enhance the amplitude and frequency of the blunt body vibration. The proximity effect and wake interference in the dual blunt body capture structure can effectively increase the vibration displacement and frequency of the blunt body, thus improving the capture characteristics of the eddy current-induced vibration capture device.

In recent years, an increasing number of researchers have embraced Computational Fluid Dynamics (CFDs) methods for analyzing two-phase flow and fluid–structure interactions. Notable advancements include the uniform mixed flow model for gas–liquid two-phase flow [19], the Shear Turbulence Profile (STP) method for examining boundary layer shear variations [20], the Smoothed Particle Hydrodynamics (SPHs) control method

for robust fluid–solid coupling [21], and a three-dimensional mixed dynamics model designed for CFDs-DEM coupling [22]. These research developments underscore the potential of CFDs numerical techniques in addressing complex fluid dynamics challenges, as well as recent strides made in enhancing computational efficiency and the accuracy of the results.

Figure 1 is a model of a double cylindrical blunt body vortex-induced vibration power generation system; the structure of the device mainly consists of a double cylindrical blunt body, transmission structure, and a linear generator with three parts. Among them, the double cylindrical blunt body and the spring assembly form a vortex-induced vibration-capturing structure; the upper cylindrical blunt body is rigidly connected to the transmission structure, and the lower cylindrical blunt body is placed on two slides to prevent the blunt body from rotating in the water and affecting the vortex generation. Compared with the traditional VIVACE device, the structure mentioned in this paper eliminates the complex transmission structure, such as gears and conveyor belts, which reduces the loss in the energy transfer process. The electric energy conversion part is a linear generator with a Halbach magnet structure, which improves the air gap magnetic flux density and facilitates an increase in the amplitude of the vortex-induced vibration motion and the conversion of electric energy.

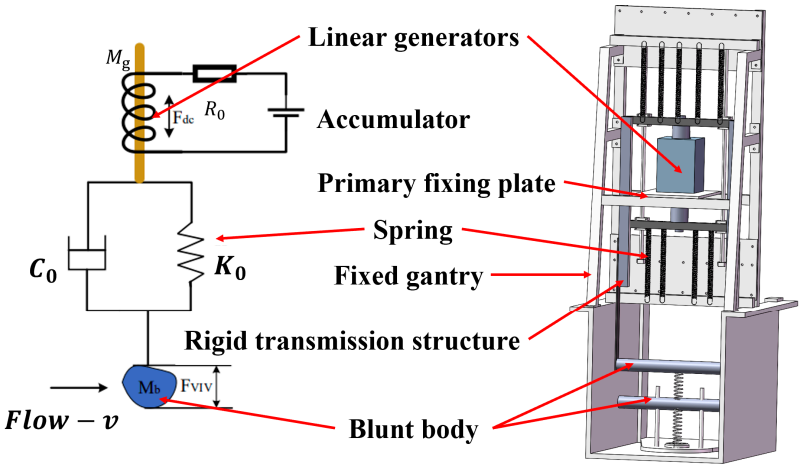


Figure 1. Equivalent model and physical structure of vortex-induced vibration power generation system.

This paper proposes a vortex-induced vibration power generation technology based on a double cylindrical blunt body. Firstly, the characteristics of the vortex-induced vibration of the cylindrical blunt body with different flow velocities, different spacing of the blunt body, and different densities of the blunt body and other parameters are analyzed by using the CFDs numerical calculation method. The amplitude, frequency, and average lift of vortex-excited vibration and the vortex shedding mode in the flow field are simulated to calculate the efficiency of the vortex-excited vibration capture of ocean current energy. Then, the self-developed linear generator is combined with the double cylindrical blunt body vortex-excited vibration system to form a complete experimental prototype of a vortex-excited vibration power generation system. Real experiments in the speed range of 0.2–0.8 m/s verify the conversion efficiency of the system.

2. Mathematical Models

2.1. Equations of Motion

The vortex-induced vibration response is an effective and critical step in converting low-flow velocity water flow energy into vibrational mechanical energy. Based on the theory of fluid–solid coupling vibration, a mathematical model of a vortex-induced vibration capture system is established, and the theoretical reference of this part is shown in the contents of Appendix A. This paper focuses on the incompressible flow of a Newtonian fluid of constant density ρ_f around two identical cylinders arranged side-by-side. The fluid

domain is modeled as laminar flow with gravity conditions imposed, and the incompressible Navier–Stokes equations for momentum conservation and the continuity equations for mass conservation are formulated as follows:

$$\rho_f \frac{\partial u_{fluid}}{\partial t} + \rho_f \left(u_{fluid} \cdot \nabla \right) u_{fluid} = \nabla \cdot [-pI + M] + F_f + \rho_b g \tag{2}$$

$$\nabla \cdot u_{fluid} = 0 \tag{3}$$

$$M = \mu_f \left[\nabla u_{fluid} + \left(\nabla u_{fluid} \right)^T \right] \tag{4}$$

where ρ_f is the fluid density; ρ_b is the density of the cylindrical blunt body; u_{fluid} is the velocity field of the water flow ($u_{fluid} = U_{fluid} n$, n is the boundary normal); I denotes the unit meridian; F_f denotes the volumetric force affecting the fluid; μ_f is the hydrodynamic viscosity; and p is the fluid pressure.

The equivalent model of the vortex-induced vibration power generation system shown in Figure 1 can be equated to a vibration system containing spring–mass–damping. Only one degree of freedom vortex-induced vibration phenomenon is considered since the transverse amplitude of the cylinder is significantly higher than the flow amplitude [8,23]. The double cylindrical blunt body structure treated as a spring–mass–damping system can vibrate in the y-direction perpendicular to the flow velocity. Based on this, the dynamic motion of a cylinder subjected to hydrodynamic forces has the following vibration control differential equation:

$$\rho_b \frac{\partial^2 y}{\partial t^2} = \nabla \cdot (BZ)^T + H_v \tag{5}$$

$$B = O + \nabla y \tag{6}$$

$$\ddot{y} + \frac{4\pi\xi}{U_r}\dot{y} + \frac{4\pi^2}{U_r^2} y = \frac{C_L}{2m^*} \tag{7}$$

where $\ddot{y}$, $\dot{y}$, and y are the transverse acceleration, velocity, and displacement of the cylinder; B is the deformation gradient; Z is the type II Piola–Kirchhoff stress; H_v is the volumetric force vector; O is the equivalent tensor; ξ is the structural damping ratio; C_L is the coefficient of lift; and U_r denotes the approximation velocity, which in this study is defined as $U_r = U_{fluid}/(f_n D)$, where f_n is the intrinsic vibration frequency of the cylinder in the water. The MUMPS solver solves the vibration control differential equations. The PARADISO solver solves the pressure–velocity coupling. All the decomposers are based on LU decomposition.

2.2. Vortex-Induced Vibration Energy Conversion Model

The capture efficiency of vortex-induced vibration is the ratio of the mechanical energy of the vibration to the total fluid mechanical energy acting on the oscillator. The fluid power is the product of the dynamic pressure head and the volumetric flow rate of the water stream, which is proportional to the square of the flow rate, and the total fluid power P_f generated by the water flowing through the blunt body can be obtained:

$$P_f = \frac{1}{2}\rho_f {U_{fluid}}^3 (2A + D) L \tag{8}$$

where D is the diameter of the cylindrical blunt body, A is the vibration amplitude of the vibrator, and L is the characteristic length of the blunt body. The vortex excitation force F_{VIV} of the fluid on the blunt body during the vibration of the oscillator contains two forces, i.e., the drag force and the lifting force, expressed as follows:

$$F_L = \frac{1}{2} c_y \rho_f \ddot{y} S, \; F_D = \frac{1}{2} c_d \rho_f \ddot{y} S \tag{9}$$

where c_y is the lift coefficient, c_d is the drag coefficient, and S is the force area of the oscillator perpendicular to the direction of the incoming flow, where $S = DL$. The force on the additional mass can be equated to $m_a a$, and a is the vibrational acceleration of the fluid. The external force F on the oscillator is as follows:

$$F = F_L - F_D - m_a a \tag{10}$$

The energy conversion efficiency η_{of} is calculated as follows:

$$\eta_{of} = \frac{P_{VIV}}{P_f} = \frac{\int_0^T F \cdot \dot{y} dt}{\frac{1}{2} T \rho_f {U_{fluid}}^3 (2A + D) L} \tag{11}$$

The electrical energy conversion efficiency of a vortex-induced vibration power generation system is the ratio of the electrical energy output of the generator to the captured flow energy:

$$\eta_{electric} = \frac{P}{P_f} = \frac{V^2/R}{\frac{1}{2} T \rho_f {U_{fluid}}^3 (2A + D) L} \tag{12}$$

V is the voltage rms value, and R is the load resistance. Combining the above equations, it can be obtained that the capture efficiency of the vortex-induced vibration device is closely related to the vibration displacement, vibration velocity, vibration acceleration of the oscillator, fluid flow rate, mass of the blunt body, vibration damping and stiffness, and the size of the blunt body and other parameters.

3. Simulation Analysis

The vortex-induced vibration response is closely related to the blunt body characteristics and fluid characteristics. Changes in blunt body and fluid characteristics directly affect the magnitude of Reynolds number Re, affecting the vortex shedding frequency, shedding velocity, and pressure distribution. Therefore, it is necessary to investigate the blunt body density, spring stiffness, and water velocity. Several important factors may be decisive in determining the VIV characteristics, including the density ratio (ρ^*) and the spacing ratio (S/D, with S being the center distance between the two blunt bodies), and the Reynolds number (Re) is defined in terms of its reference quantity: $Re = \rho_f U_{fluid} D / \mu_f$. The specific parameters are defined as shown in Table 1:

Table 1. Blunt body and fluid characterization parameters.

Description	Symbol	Value
Fluid density	ρ_f (kg/m^3)	1×10^3
Fluid power viscosity	μ_f (Pa·s)	1.01×10^{-3}
Uniform incoming velocity	U_{fluid} (m/s)	0.2–0.8
Rate of approximation	U_r	3.633–14.532
Density ratio	ρ^*	3.5–8.5
Diameter of blunt body	D (mm)	50
Effective length of blunt body	L (mm)	450
Blunt body intrinsic frequency	f_n (Hz)	1.101
Coefficient of spring elasticity	K (N/m)	30–80

3.1. Computational Domains and Mesh Profiles

From the computational domain shown in Figure 2, the lengths of the computational domain in the x-direction and y-direction are 65D and 30D, respectively. The computational domain is divided into three parts (the blunt body motion domain, the wake domain, and the external flow field domain). The double cylindrical blunt body is placed side-by-side in the positive direction of the y-axis, and two circles combine the kinematic domain near the cylinder with a radius of 1.7D, which is convenient for the subsequent mesh dissections to be more refined and improve the convergence of the model.

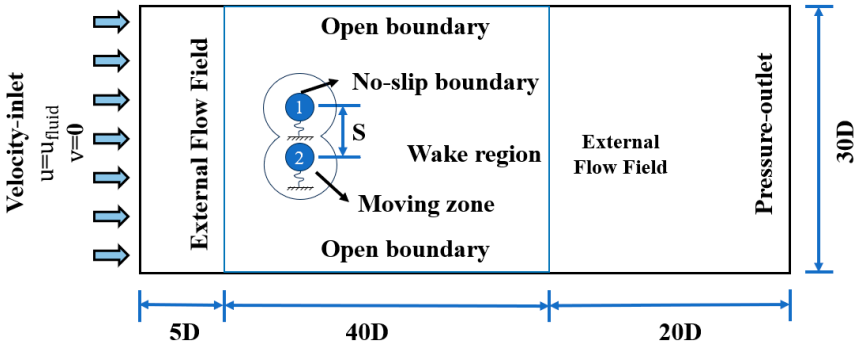


Figure 2. Simulation computational domain and boundary conditions.

The computational domain comprises four boundaries (inlet, outlet, sidewalls, and cylindrical blunt body walls). The inlet is set up as a normal inflow velocity field, and the water flow is uniform throughout the computational domain. In order to improve the convergence of the calculation, a static pressure condition is set at the outlet boundary. At the outlet boundary, the above equations are supplemented with the boundary conditions $[-pI + M]n = -\hat{p}_0 n$ and $\hat{p}_0 \leq p_0$, where p_0 is the absolute pressure at the boundary, to reduce the amount of fluid entering the domain at the boundary by suppressing the backflow and minimizing the impact on the near wake region of the cylindrical flow. In addition, open boundary conditions are applied to the top and bottom sidewalls, and no-slip conditions are imposed on the cylinder surface.

This paper uses a dynamic mesh approach to reconstruct and update the mesh using the Yeoh smoothing method. As shown in Figure 3, the mesh arrangement is near a double cylindrical blunt body. An unstructured mesh is used in the circular region of the computational domain. In order to solve the problem of the high resolution of the flow characteristics around the cylinder, a flow boundary layer is set up in the near-wall region of the cylinder, and a free triangular mesh refinement is performed in its vicinity with a maximum cell size of 0.0091 m. In addition, only the double-circular combination region is defined as the dynamic mesh region to improve computational efficiency. When external fluid forces act on the cylinder, the cylinder oscillates and the mesh is reconstructed to improve model convergence and computational accuracy.

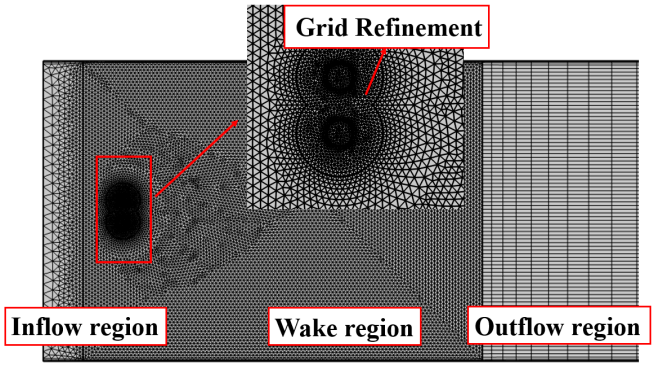


Figure 3. Mesh sectional drawing.

In order to obtain reliable computational results, it is important to ensure that the mesh density and time step are sufficiently appropriate. Simulations of vortex-induced vibration were carried out for a double cylindrical blunt body at Re = 25,000. A comparison of the dimensionless transverse amplitude (Y/D), frequency ratio (f/f_n), and average resistance results is given in Table 2. The dimensionless transverse vibration amplitude is defined as $Y/D = (Y_{max} - Y_{min})/2D$, where Y_{max} and Y_{min} denote the maximum and minimum displacements of the cylinder, respectively. The numerical results have good convergence

as the maximum grid cell length decreases, the number of cells increases, and the time step decreases. The maximum percentage change (7.6%) occurs at the f/f_n value when the grid changes from A1 to A2, whereas no significant change is observed when the grid changes from A2 to A3 (only 0.1% change in the f/f_n value). Thus, the comparison shows that case A2 is fully plausible and can be used for subsequent validation.

Table 2. Mesh independence study and time refinement study of a double cylindrical blunt body.

Operating Cases	Maximum Grid Cells (m)	Number of Cells	Time Step	*Y/D*	f/f_n	Average Lift (N/m)
A1	0.01	27,914	0.05	55.713	2.38	19.723
A2	0.091	28,238	0.05	55.434 (−0.5%)	2.56 (7.6%)	19.743 (0.1%)
A3	0.081	33,582	0.05	55.626 (−0.16%)	2.4 (0.1%)	19.874 (0.77%)
B1 (A2)	0.091	28,238	0.05	55.434	2.38	19.743
B2	0.091	28,238	0.03	55.883 (0.8%)	2.32 (−2.5%)	19.861 (0.6%)
B3	0.091	28,238	0.01	55.383 (0.01%)	2.38 (0%)	19.807 (0.3%)

3.2. Simulation Analysis of Vortex-Induced Vibration Response of Single Blunt Body

Based on the above computational domain and mesh dissections, simulation analyses of vortex-induced vibrational energy capture of a single blunt body are carried out, and the effects of the density ratio of the blunt body ($3.5 \leq \rho^* \leq 8.5$) and the elasticity coefficient ($30 \leq K \leq 80$) on the vibration amplitude and frequency of the cylindrical blunt body are discussed, with the velocity of the water flow approximation being a fixed value ($U_r = 14.532$) and the dimensionless vibration amplitude being defined as $Y/D = (Y_{max} - Y_{min})/2D$, where Y_{max} and Y_{min} denote the maximum and minimum displacements of the cylinder, respectively.

As shown in Figure 4, the vibration amplitude curve is analyzed in detail. When the spring elasticity coefficient is in the range of $30 \leq K \leq 60$, the dimensionless vibration amplitude Y/D shows a tendency of increasing and then decreasing with the density ratio ρ^*, and there exists a point of great value near $\rho^* = 0.4$, at which time the maximum peak of Y/D is 0.521; when the spring elasticity coefficient is in the range of $70 \leq K \leq 80$, the vibration amplitude Y/D shows a linear decreasing trend with the increase in the density ratio. In the whole density ratio interval, although the vibration amplitude has a slight fluctuation within a certain range, the overall trend is decreasing; in order to obtain a larger amplitude of vibration displacement, the density of the blunt material should be as small as possible.

The above analysis shows that the change rule of the vibration amplitude will be affected by the elasticity coefficient. When the density ratio of the blunt body is in the range of $0.35 \leq \rho^* \leq 0.65$, with the increase in the elasticity coefficient, Y/D shows the trend of increasing first and then decreasing; the amplitude of Y/D in the case of K = 60 is generally higher than the other curves, and in the interval of $\rho^* \geq 0.7$, under the condition of the same density ratio, the vibration displacement shows a trend of linear growth with the increase in the spring's elasticity coefficient K. At this time, the points on the K = 80 curve are higher than the other curves. Therefore, different densities of blunt bodies need different elasticity coefficients of the spring in order to achieve the maximum vibration amplitude.

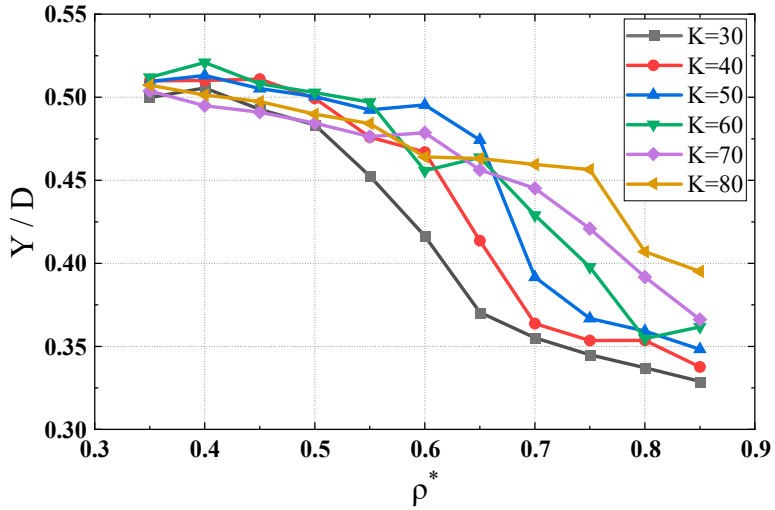


Figure 4. Vibration amplitude variation curve of single blunt body.

Figure 5 shows the single cylindrical blunt body vibration frequency with the ρ^* and K change rule. With the increase in the elasticity coefficient K, the cylinder vibration frequency shows a linear increase trend; the larger the spring elasticity coefficient, the more favorable the chance of increasing the vibration frequency of the blunt body, which helps to improve the water flow energy capture. As for the density ratio ρ^*, the vibration frequency f/f_n decreases with the increase in ρ^*, and maximum frequency occurs in the case of K = 80 and $\rho^* = 0.35$, when f/f_n is 4.367 at the maximum, which is 1.25 times higher than the minimum vibration frequency. From the analysis of Figures 4 and 5 above, it can be seen that the vibration amplitude and frequency are higher when the value of ρ^* is smaller, but when the elasticity coefficient K is larger, the vibration amplitude attenuation is serious and the vibration frequency rises. So, the density ratio $\rho^* = 0.4$, K = 60 for the cylindrical blunt body movement is more ideal, based on this condition for analyzing the later vortex vibration motion.

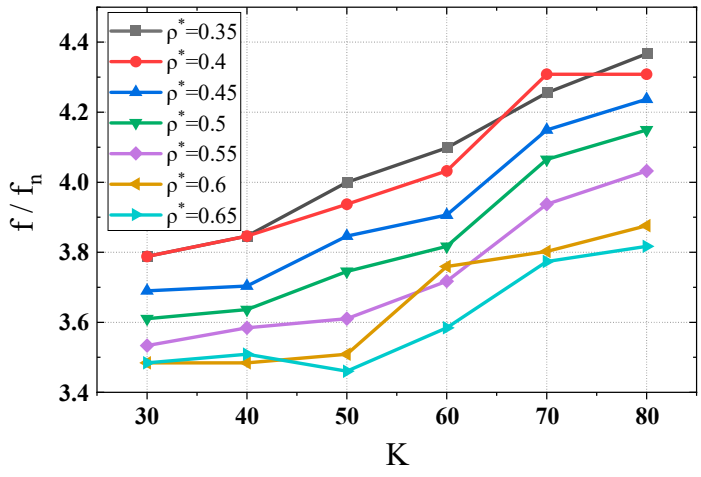


Figure 5. Single blunt body vibration frequency variation curve.

As shown in Figure 6, the optimal combination of the density ratio of the blunt body and the elasticity coefficient is selected from the previous section, and the trends of the cylindrical vibration amplitude Y/D and vibration frequency f/f_n are analyzed by changing the water flow velocity. The range of approximate velocity $3.6 \leq U_r \leq 8.2$, with the increase in water velocity, Y/D shows a rapidly increasing trend, and the peak displacement is 0.588 at $U_r = 8.17$. The reason for the rapid increase in vibration displacement is that the cylindrical vibration frequency $f/f_n \geq 1$ in the velocity interval, that is, the frequency of

vortex shedding is close to the intrinsic vibration frequency of the vibrating cylinder with the stationary water, and at this time, the resonance phenomenon will occur, so that the cylindrical amplitude is dramatically enhanced, and this interval is usually defined as the locking zone [24,25]; in the range of $8.2 \leq U_r \leq 14.5$, Y/D shows a slow decreasing trend, the reason being that the acceleration of the water flow speed increases the vibration frequency, and at the same time it generates harmonics with different frequencies to suppress the size of the cylinder amplitude, but the vortex excitation force of the water flow it resists is still increased.

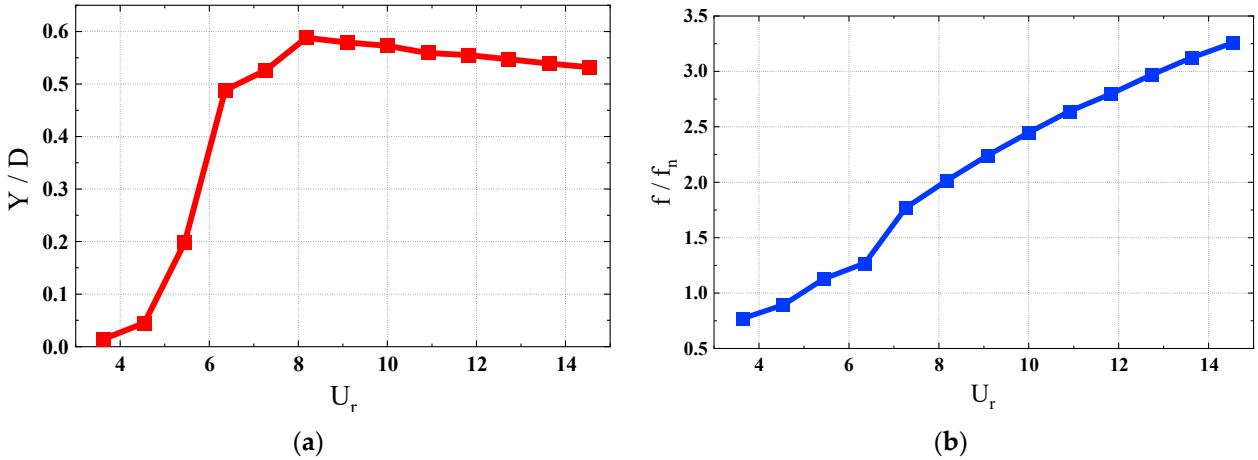


Figure 6. Trend curve of vortex-induced vibration motion of single blunt body with changing flow velocity: (**a**) vibration amplitude variation curve; (**b**) vibration frequency variation curve.

4. Simulation and Analysis of Vortex-Induced Vibration Response of Double Blunt Body

4.1. Vibration Amplitude and Frequency

The characteristic parameters of the blunt body and the fluid are determined by analyzing the vortex-induced vibration response of a single cylindrical blunt body. In order to compare the enhancement of the side-by-side double blunt body structure in capturing the energy of the water flow, the vortex-induced vibration of the double blunt body is simulated and analyzed under the same working condition, and the density ratio of the cylinder is selected as $\rho^* = 0.4, K = 60$. In order to have a better chance of the vortex-induced vibration phenomenon occurring, the conditions set in the simulation are all ideal. Compared with the case of a single cylinder, the fluid–solid coupling problem of a double cylindrical blunt body in water is more complicated. A previous study found a proximity effect when the center spacing ratio S/D is small. The wake interference also affects the vibration response when S/D is large. As shown in Figure 7, since the vortex-induced vibration response of two cylinders placed side-by-side vibrates symmetrically over most of the range of U_r, only the response state of the upper cylindrical blunt body is shown in the following analysis.

In order to investigate the effect of the center spacing ratio on the vibration response of side-by-side double cylinders, all the response simulations in the range of U_r are required. As shown in Figures 8 and 9, by varying the approximate water flow velocity U_r and different center spacing ratios S/D, the graphs of vibration amplitude and frequency change in the VIV motion response of the double cylindrical blunt body. When $S/D \leq 2.4$, the interaction force between the two cylinders is more extensive, and the vibration amplitude reaches the maximum value $Y/D = 0.59$ at S/D = 2.2, which improves the amplitude by 1.04 times compared with the single blunt body structure. The amplitude response increases significantly at $U_r = 5.45$, when the interaction force between the cylinders makes the cylindrical vibration frequency enter the locking interval in advance, and the range of the large amplitude region of the cylindrical passivate body is wider than that of the

case of S/D > 2.4. When the center spacing is wider than S/D > 2.4, the width of the large amplitude region of the double cylindrical blunt body placed side-by-side decreases with the increase in S/D, the region is almost unchanged after S/D > 3.4, and the interaction force between the two blunt bodies becomes weaker, which is similar to that of the two single cylindrical blunt bodies.

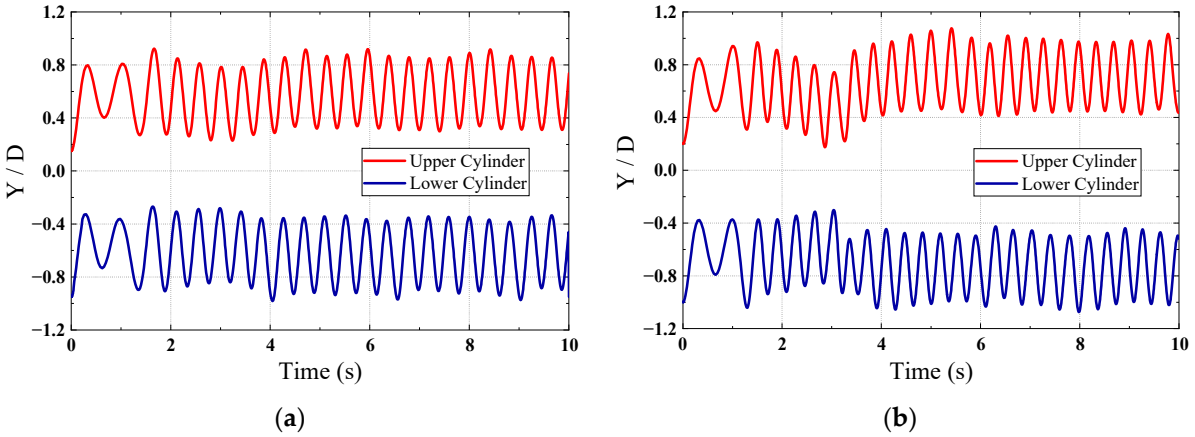


Figure 7. Vibration displacement curve of double cylindrical blunt body: (**a**) center spacing ratio S/D = 2.2; (**b**) center spacing ratio S/D = 2.4.

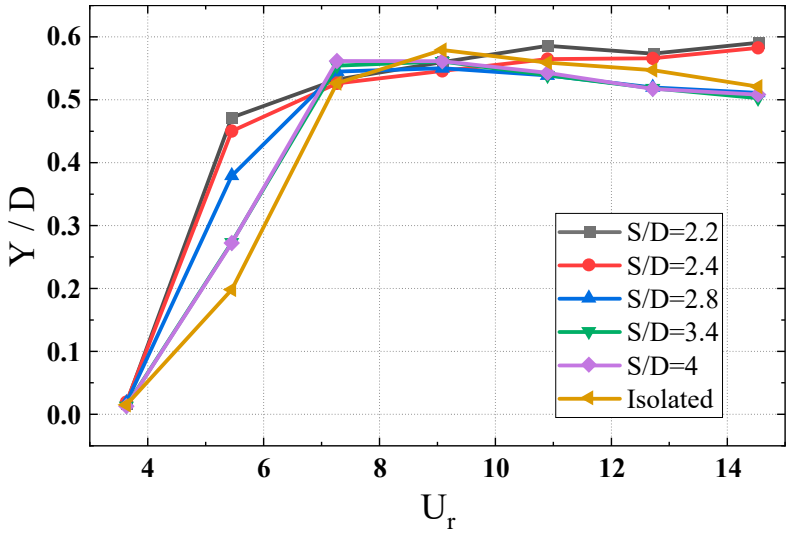


Figure 8. Double blunt body vibration amplitude variation curve.

The double cylindrical blunt body structure is higher than the single blunt response amplitude for most of the range of U_r. However, the cylindrical vibration amplitude is smaller than that of the single cylindrical blunt body at U_r > 7.27. This phenomenon is caused by the interference of the interstitial water flow between the cylindrical blunt bodies, which exhibits a strong nonlinear effect, thus inducing multiple frequencies and reducing the amplitude. In the case of the double cylindrical blunt body, the peaks of S/D = 2.8, 3.4, and 4 occur at almost the same U_r. It is noteworthy that the double cylindrical amplitude response is almost similar to the single cylindrical response at U_r = 3.63 and 7.27, with U_r = 3.63 being the onset of vortex-induced vibration and U_r = 7.27 being the transition point at which the rapid increase in amplitude becomes slow. The study found that the highest amplitude of 0.59D is less than half of the center distance ratio, and the two cylindrical blunt bodies do not collide.

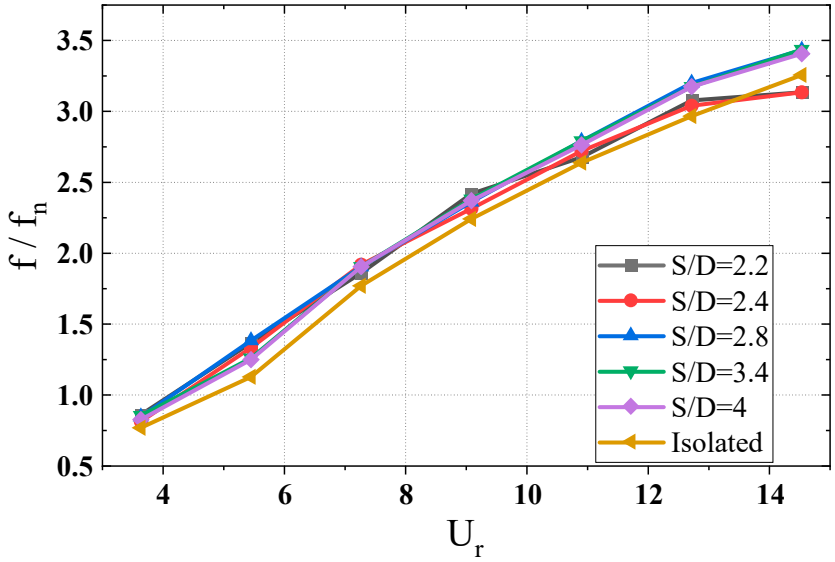


Figure 9. Frequency variation curve of double blunt simulation.

In the case of a single cylindrical blunt body, the vortex-induced vibration is only vortex shedding. However, in the case of double cylinders placed side-by-side, the vortex-induced vibration also comes from the gap flow between the two cylinders. The smaller gap ratio will increase the fluid flow between the cylinders as well as the vortex shedding frequency, as shown in Figure 9. The trend of the vibration frequency of the double-cylinder blunt and single-cylinder blunt is basically the same. The frequency f/f_n increases with the increase in the approximation velocity U_r for different center distance ratios S/D. Although the larger center distance ratio S/D makes the cylindrical vibration displacement not as good as that of the single-cylinder obturator, the wake interference phenomenon still makes the vibration frequency increase so that the side-by-side double-cylinder obturator appears to be a locking or synchronization phenomenon earlier. The earlier appearance of the locking region is also accompanied by a high vibration amplitude response, which is beneficial to the conversion of mechanical energy in a wide range of water flow velocities. Energy harvesting devices such as the VIVACE require high vibration amplitude and frequency to increase the efficiency of converting kinetic energy into mechanical energy.

4.2. Motion States and Energy Transitions

The tendency of the isotropic motion of the cylinders can be clearly seen from the displacement curves in Figure 7a. Figure 10 illustrates the vorticity curves for the isotropic motion of the double cylindrical blunt body at different moments. The gap between the two cylinders is maintained at a constant value, resulting in a nearly constant gap flow. When the two cylinders move downward from the top (Figure 10a–c), the inner vortex of the upper cylinder moves upward. It separates the free side vortex into two parts, and the free side vortex of the lower cylinder merges upward and pairs with the inner vortex of the upper cylinder. However, as both cylinders move upward from the bottom (Figure 10d–f), the free side vortex of the lower cylinder separates and, due to the influence of the free side vortex of the upper cylinder, the inner vortex of the upper cylinder is split into two parts, one of which is paired with the free side vortex. The process is related to the vortex-shedding process studied by Chen et al. [26]. From Figure 11, it can be seen that when the in-phase vortex shedding mode occurs, there is no significant increase in the peak lift, but the average lift reaches 20.98 N compared to the single blunt body structure by a factor of 1.08.

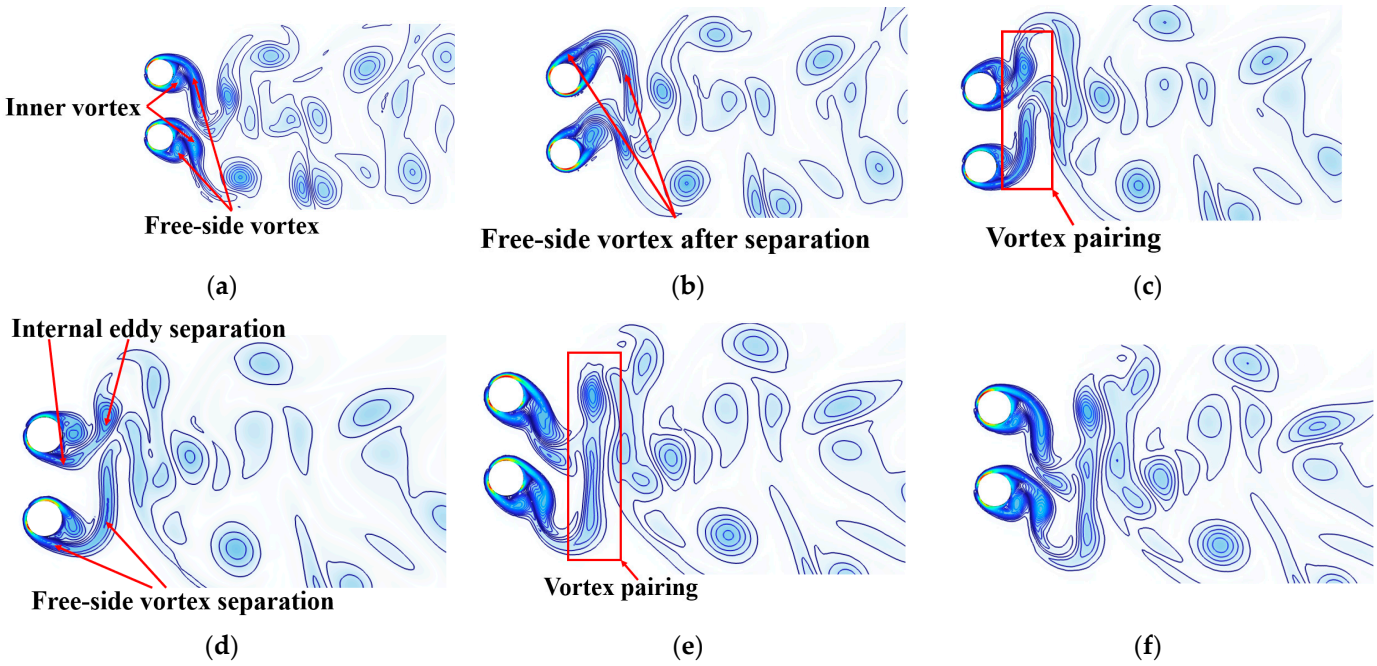


Figure 10. Vorticity profiles of double blunt bodies moving in the same direction at different moments of time (S/D = 2.2): (**a**–**c**) show the synchronised ascending motion; (**d**–**f**) show the synchronised descending motion.

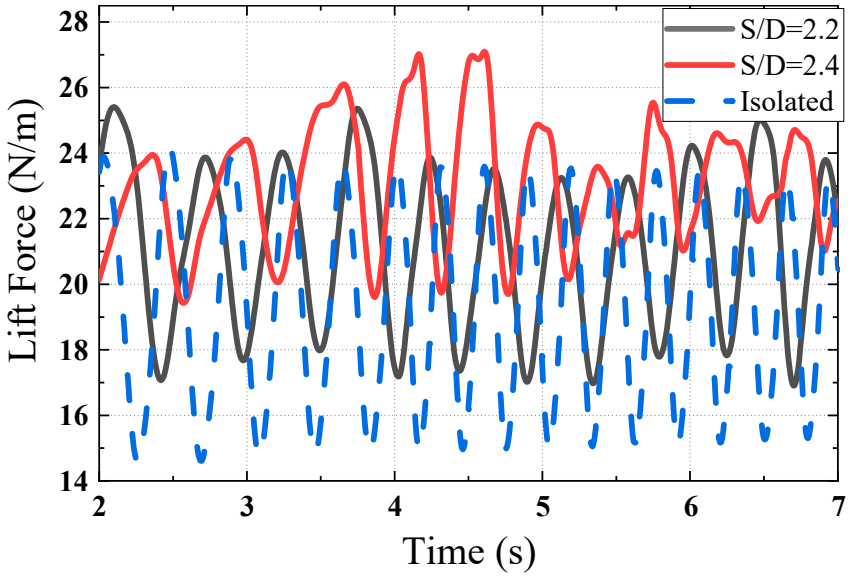


Figure 11. Variation curve of the lift coefficient for different blunt body spacings.

Figure 12 shows a dual cylindrical blunt body inverse vortex shedding pattern, where the vortices of the upper and lower cylinders are shed in the opposite directions, and the gap between the side-by-side cylinders will become smaller as the upper cylinder moves downward and the lower cylinder moves upward, so the fluid flow within the gap will increase and the pressure response will decrease. The pressure drop within the gap will significantly increase the lift of the vibrating cylinders. The intense interaction between the internal vortex and the free side vortex leads to irregular lift and poor displacement–lift correlation. As shown in Figure 11, the cylinder lift curve does not have ideal sinusoidality when S/D = 2.4, and when compared with the displacement curve in Figure 7b, the interaction force between the cylinders is enhanced in the time range of 2–4 s with the gap

decreasing. However, the lift curve has a maximum peak in the period of 3–5 s, which has a certain ability of phase lag phenomenon. Compared with the single blunt body lift curve, the maximum peak lift of the double blunt body is 27.1 N, which is increased by 1.14 times, and the average lift is 23.15 N, which is increased by 1.2 times. The previous energy conversion efficiency formula shows that the maximum conversion efficiency of the vortex vibration energy is 83.3%.

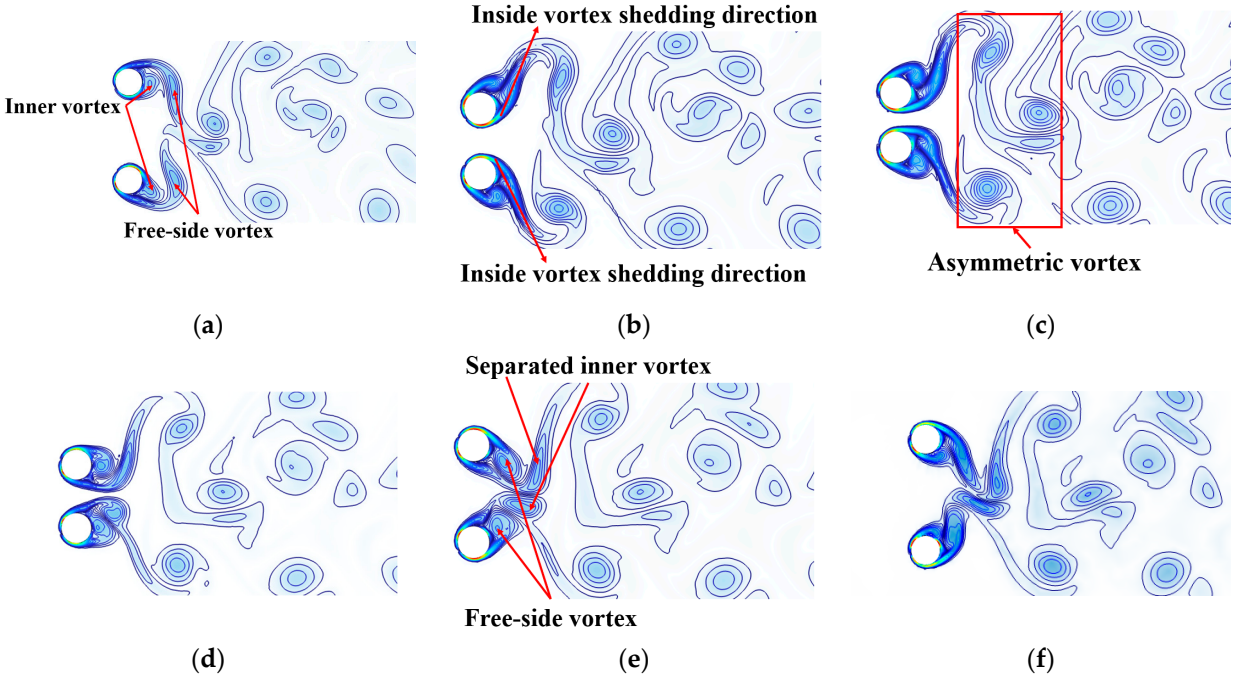


Figure 12. Vorticity profile of the reverse motion of the double blunt body at different moments of time (S/D = 2.4): (**a**–**c**) show the motion of the double columns approaching to the inside; (**d**–**f**) show the motion of the double cylinders separating to the free side.

5. Experimental Validation

In order to simulate the uniform fluid flow in the ocean, a circulatory flow type tank, as shown in Figure 13a, has been constructed in the laboratory. It includes a rectification section, a test section, and a power control system. The flow velocity in the frequency range of 0–50 Hz was tested by using a tachometer and setting the sampling period to 5 min to calculate the average value of the flow velocity during the sampling period. The installation position of the tachometer is shown in Figure 13b. The relationship between the flow velocity and the frequency of the inverter was measured at water depths of 0.15 m, 0.3 m, and 0.45 m, respectively. The test results are shown in Figure 14. The flow velocity at different depths and the frequency of the inverter satisfy the law of linear change, and the flow velocity is relatively low under the condition of greater water depth. The flow velocity range in the test section is 0.2–0.8 m/s, the instability of the flow velocity is less than 1%, and the whole can fulfill the conditions of the water flow velocity of the vortex-induced vibration power generation system. Therefore, when the vortex vibration capture experiment is carried out in the circulating water tank, the initial position of the blunt body should be selected as the appropriate water depth in the tank.

From the above simulation results, it can be seen that in the double cylindrical blunt body, in the case of a smaller center spacing ratio S/D, the interaction between the cylinders is more extensive. The proximity effect increases the amplitude and frequency of the cylinders, so laboratory flume experiments are selected to discuss the vibration of the cylinders in the three cases of S/D = 2.2, 2.4, and a single blunt body. The laboratory double blunt body vortex-induced vibration power generation system is shown in Figure 15.



Figure 13. Laboratory circulating water tank physical image: (**a**) circulating flow type water tank physical picture; (**b**) flow meter test position.

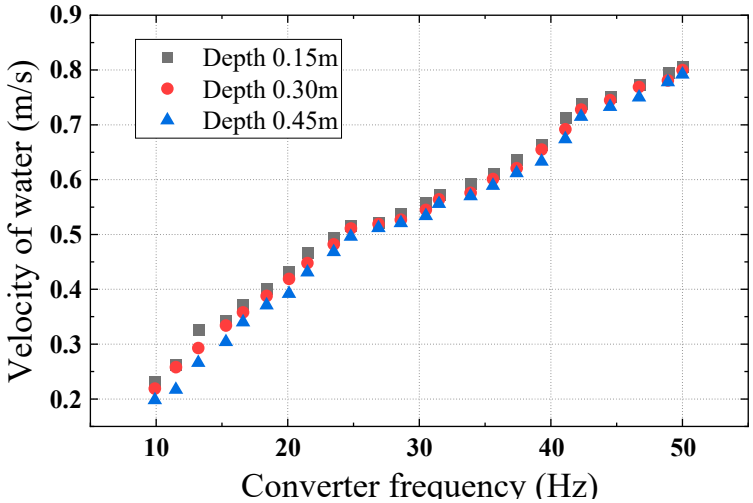


Figure 14. Frequency of frequency converter and water flow rate curve.

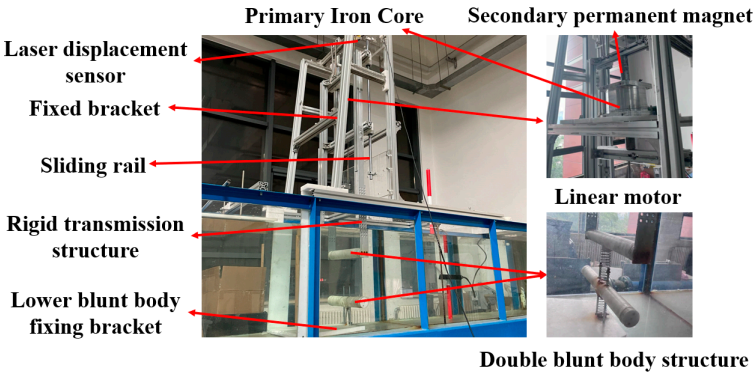


Figure 15. Physical drawing of circulating water tank test device.

The vortex-induced vibration power generating unit is divided into three parts, as shown in Figure 15. The lower part is a double cylindrical blunt body vortex-induced vibration-capturing device. The upper cylindrical blunt body is rigidly connected to the transmission structure by two perforated steel plates to ensure that the blunt body moves in the transverse direction of the water flow and transmits the vibration mechanical energy to the linear motor. The lower cylindrical obtuse body is fixed to the lower fixed frame by two sliding rails because the two cylindrical movements exist in the same direction and reverse two kinds of movement states, so the lower cylindrical blunt body only plays

the role of reinforcing the vortex-induced vibration movement. It is not connected to the transmission structure. The transmission structure connects the upper cylindrical obtuse body and the linear motor secondary magnet to ensure the consistency of the movement of the obtuse body and the secondary magnet, which is supported by two sliding guide rails to ensure the verticality of the whole device, and no inter-structural deformation occurs. The linear generator consists of the primary iron core and the secondary permanent magnet. The primary iron core is fixed on a fixed bracket with multi-turn coils wrapped inside to cut magnetic force lines and convert electrical energy. The secondary magnet of the linear generator is partially fixed inside the transmission structure, connecting the blunt body and the motor into one part to minimize the loss in the energy transmission process. When the cylindrical blunt body undergoes periodic vibration, it directly drives the secondary side of the linear motor to move and realize electric energy conversion. A laser displacement sensor is installed at the top to measure the amplitude and vibration frequency of the cylindrical blunt body.

Figure 16 shows the influence curve of a different flow velocity on the vibration displacement and frequency of the passivate body; from the overall trend, the vibration displacement curve of the two sets of devices all show the trend of increasing and then decreasing, and due to the influence of two cylindrical proximity effects, the double passivate body structure reaches the peak value in advance at a flow velocity of 0.527 m/s. The vibration frequency shows the same increasing trend, and with the increase in flow velocity and vibration frequency acceleration, double cylindrical obtuse body structure vibration displacement and frequency are generally higher than the single cylindrical obtuse body. From the specific analyses in Figure 16a, it can be seen that in the single cylindrical blunt body capture structure, the large amplitude region is 0.527 m/s $\leq U_{fluid} \leq$ 0.655 m/s within the flow velocity range, and the maximum vibration displacement of 105.992 mm occurs at a flow velocity of U_{fluid} = 0.564 m/s. The maximum vibration displacement of 105.992 mm occurs at a flow velocity of U_{fluid} = 0.564 m/s. The maximum vibration displacement of 105.992 mm occurs at a flow velocity of 0.564 m/s. For the double cylindrical blunt capture structure, the vibration displacement is larger than that of the single cylindrical blunt capture structure at different flow velocities, indicating that the ability of the double cylindrical blunt capture device to capture high-amplitude vibrations is better than that of the single blunt capture device. The double blunt capture structure has a larger vibration displacement in the flow velocity range of 0.448 m/s $\leq U_{fluid} \leq$ 0.728 m/s, which is wider than the large amplitude region of the single cylindrical passivate structure. The maximum vibration displacement occurs at S/D = 2.2, the flow velocity is U_{fluid} = 0.527 m/s, the two cylinders interfere more strongly, and the peak displacement is 118.557 mm, which is 1.12 times higher than that of the single-cylinder blunt structure. This is because the flow rate of water in the laboratory flume is not an ideal uniform flow rate, and the influence of some factors, such as the side walls of the flume, leads to a narrower locking region of the blunt body compared to the ideal case. As can be seen from Figure 16b, the cylindrical vibration frequency increases as the flow velocity increases. The vibration frequency of the double blunt body structure has a slight increase compared to the single cylindrical blunt body because the instability of the water flow makes the vortex formed in the trailing region of the cylinder have multiple harmonic frequencies, which interferes with the vortex-induced vibrational motion of the blunt body. The numerical results did not predict the experimental results very accurately. One of the possible factors contributing to this problem is that the simulation model eliminates the cylinder length effect, whereas the finite cylinder in the vortex-excited vibration experiments induces fluid flow between the cylinder tip and the channel wall.

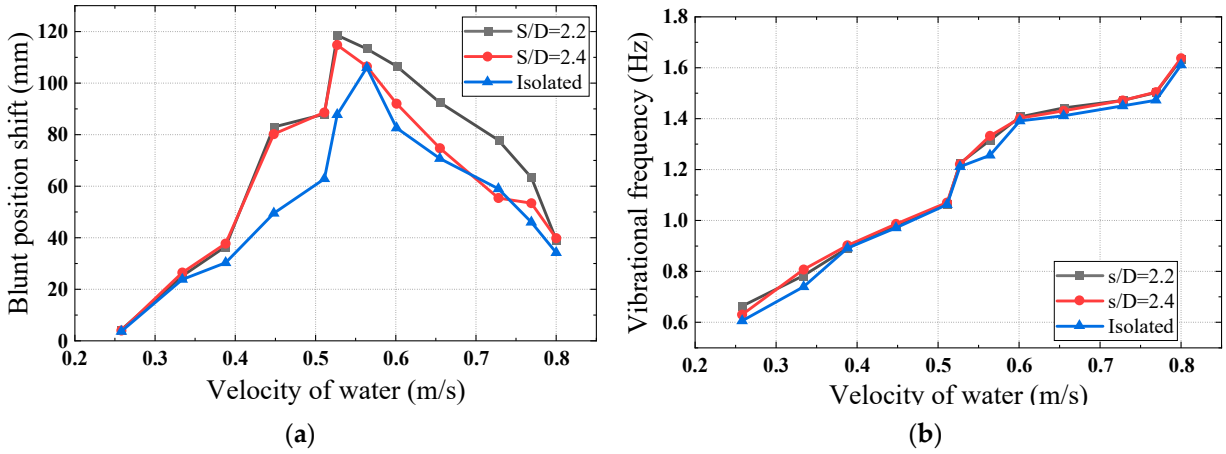


Figure 16. Motion response curves at different flow rates in a laboratory sink: (**a**) vibration displacement curve; (**b**) frequency curve.

As shown in Figure 17, the overall trend of joining the displacement curve of the motor is the same as the above for the trend of increasing and then decreasing, but due to the self-weight of the motor secondary magnet and the electromagnetic force between the magnet and the coil, the vibration amplitude in both cases has decreased, and the maximum vibration amplitude of the no-load state is relatively reduced by 5.1%. For the loaded state, the electromagnetic force of the linear motor increases dramatically after the resistance is applied, so the vortex-induced vibration needs to convert more vibration energy to ensure the normal operation of the device, and at this time, the maximum vibration amplitude decreased by 15.3%. It can also be seen from the two graphs that with the increase in the externally applied resistance, the maximum amplitude can only be reached at 0.6 m/s and 0.7 m/s for the two cases, respectively, which is an increase in the flow rate interval compared to the flow rate interval without the motor. The detailed analyses are as follows. Figure 17a shows the unloaded state; with the addition of the motor, the total mass of the vortex-induced vibration device increases, despite the use of springs to balance the weight of the linear motor, but it still adversely affects the vortex-induced vibration motion. The overall motion trend is still with the increase in flow rate; the vibration amplitude shows a trend of growth and then reduction, the double blunt body vibration amplitude is overall higher than the single blunt body structure, and the double blunt body amplitude peaks in the case of S/D = 2.2 and reached 112.11 mm. Compared with the case without linear motor amplitude (118.557 mm), this has been reduced, proving that the vortex vibration occurs by the device of the additional mass of the limitations of the device. Figure 17b shows the loaded state, adding 20 Ω load resistance; electromagnetic resistance occurs within the linear motor, which makes a part of the vortex vibration energy used to offset this part of the resistance. From the curve, we can see that with the increase in resistance, the vortex vibration power generation device starts the flow velocity from 0.2 m/s to 0.3 m/s, and the captured energy width decreases, the flow velocity is lower, and the vortex vibration force is less than the motor. When the flow rate is low, the vortex-induced vibration force is less than the motor weight and electromagnetic resistance, making the power generation device not operate normally; the maximum peak amplitude also decreased to 101.24 mm. When the flow rate reaches 0.8 m/s, the vibration amplitude decreases significantly, the flow rate is too fast, leading to the blunt body movement having a strong non-sinusoidal effect, the disturbance between the two columns is more serious, and vortex shedding does not occur regularly. There is even a phenomenon of the cylindrical stopping moving.

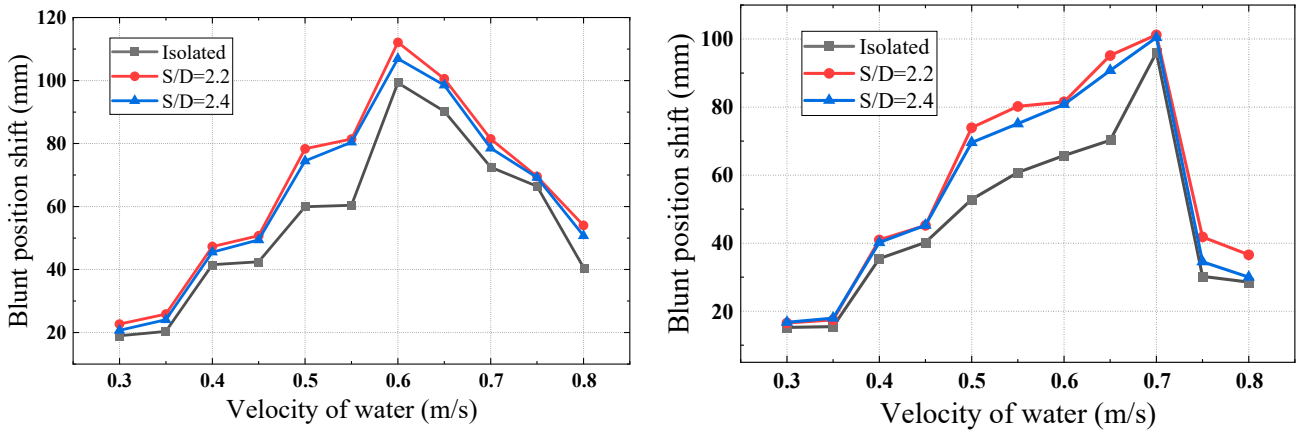


Figure 17. Vibration displacement curve of blunt body under different loads: (**a**) no-load state displacement curve; (**b**) load state displacement curve.

As shown in Figure 18 for the generator voltage amplitude under different load conditions, because the electromagnetic resistance is larger under the generator load condition, the load voltage is also smaller than the no-load voltage as a whole with the decrease in the obturator vibration amplitude, and the motor voltage amplitude shows a trend of increasing and then decreasing along with the trend of the vibration amplitude of the cylindrical obturator. As shown in Figure 18a, when the flow rate U_{fluid} = 0.6 m/s, the no-load peak voltage reaches 15.64 V, and when the flow rate U_{fluid} > 0.6 m/s, although the vibration frequency is increased, the decrease in amplitude causes the vibration speed to slow down, resulting in a reduction in the output voltage. When a resistive load is applied to the output of the linear motor, the vibration amplitude and frequency of the blunt body receive a serious suppression effect due to the increase in electromagnetic force, the total voltage amplitude is lower than the no-load state, and the peak voltage is reduced to 14.52 V, which is a reduction of 7.16%.

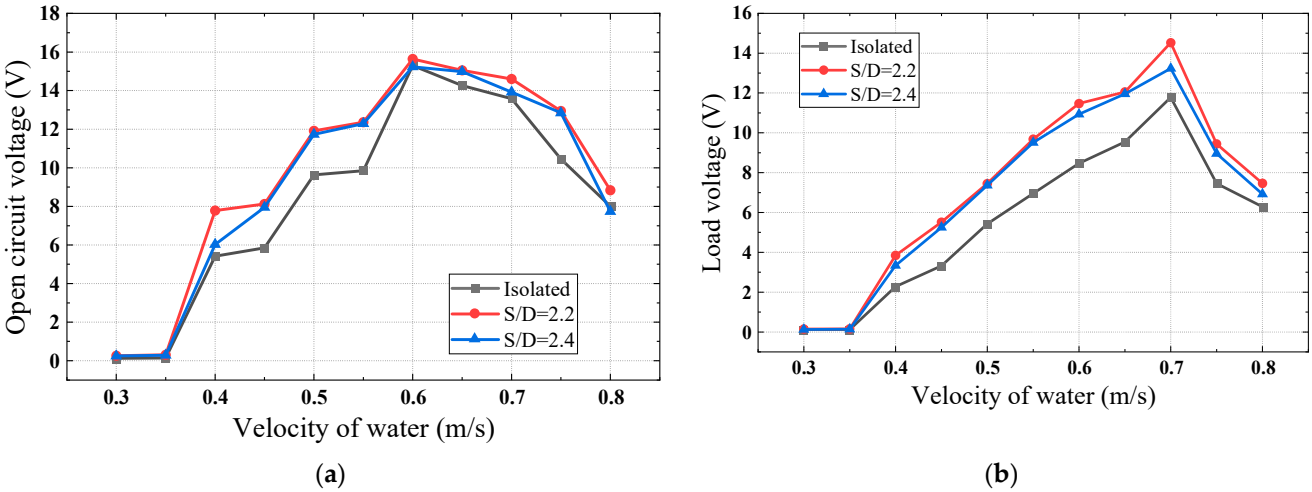


Figure 18. Voltage amplitude curves under various load conditions: (**a**) no-load voltage; (**b**) load Voltage.

6. Energy Conversion

Figure 19 shows the changing curve of output power and conversion efficiency: the load resistance value is constant, even with the increase in load voltage, the output power shows a trend of increasing and then decreasing, the output power of the double obtuse structure is higher than that of the single obtuse structure, and the maximum output power of the single obtuse structure is 1.53 times. The energy conversion efficiency can be seen

in Equation (12); because it is the relationship of the ratio between power generation and water flow energy, it is not a smooth curve, and the curve of the double obtuse structure is also higher than the single obtuse structure as a whole, and the conversion efficiency is improved by 12.33%. As shown in Figure 19a, in the range of flow velocity $U_{fluid} < 0.7$ m/s, as the flow velocity increases, the output voltage increases, and the output power of the linear generator increases, which is consistent with the voltage magnitude curve, and a maximum output power of 10.55 W is obtained at a flow velocity $U_{fluid} = 0.7$ m/s. From the curve, it can also be found that the output power of the double cylindrical blunt body is generally higher than that of the single cylindrical obturator. As shown in Figure 19b, the energy conversion is the highest when the flow velocity $U_{fluid} = 0.6$ m/s. The maximum energy conversion efficiency is 52.93%, which is not the point of the flow velocity where the output power is the largest; the reason is that with the increase in the vibration amplitude and frequency of the cylindrical blunt body, the energy conversion efficiency of the water flow is also increased. The energy conversion rate of the water flow is faster, which makes the peak point of the energy conversion efficiency and the peak point of the output power. The peak point of the energy conversion efficiency and the peak of the output power do not coincide.

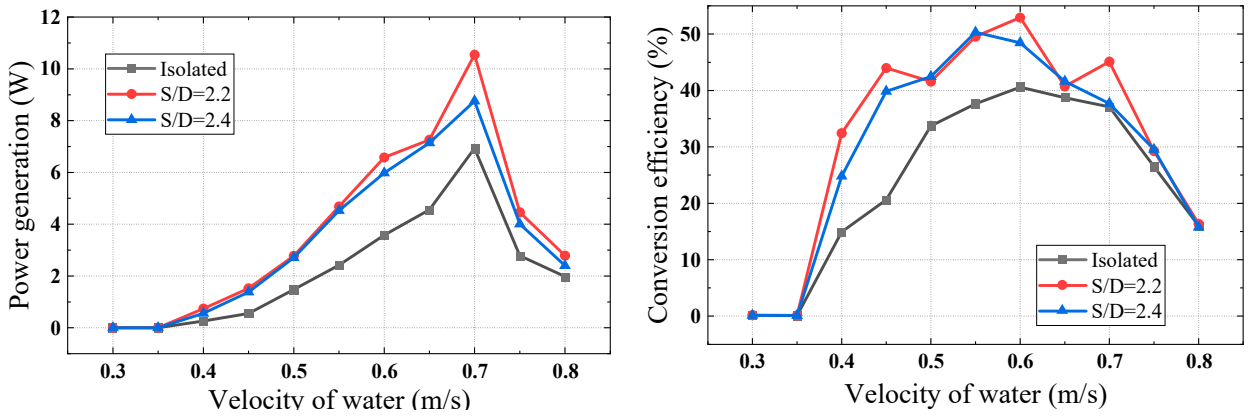


Figure 19. Linear motor output power and energy conversion efficiency curves: (**a**) output power; (**b**) electrical energy conversion efficiency.

7. Conclusions

In this paper, a vortex-induced vibration current energy capture and power generation technology based on the combination of a double cylindrical blunt body structure and a permanent magnet linear generator is proposed, which has a high conversion efficiency compared with that of a conventional turbine power generation system, especially at low ocean current speeds of less than 1 m/s. The proposed double cylindrical blunt body vortex-induced vibration current capture structure can increase vibration amplitude, frequency, and average lift compared with the single blunt body structure, thus improving the vortex-induced vibration current energy capture capability. The specific research conclusions are as follows:

(1) Based on the theory of fluid–solid coupled vibration, a CFDs mathematical calculation model of vortex-excited vibration capture is established. It is shown that the larger the periodic lift force acting on the blunt body, the higher the efficiency of converting the current energy into mechanical energy. The vortex-excited vibration response characteristics of single and double blunt body structures are simulated and analyzed. It is found that when two cylindrical blunt bodies are positioned closer together with S/D $\leq$ 2.4, the proximity effect enhances the blunt body amplitude and frequency, the Y/D can reach 0.59, and the lift force applied to the cylinder increases by

1.14 times compared with that of the single blunt body structure, which improves the vortex-excited vibration trapping efficiency.

(2) A vortex-induced vibration generation system with double cylindrical blunt bodies for laboratory sinks was developed, and the maximum vibration response amplitude obtained from the experiment reached 118.557 mm at a flow rate of 0.7 m/s, which is 1.12 times higher than that of the vibration response amplitude of a single blunt body structure. The experimental results also confirm that the double blunt structure is favorable to the improvement in the vibration amplitude of the cylindrical blunt. Combined with the self-developed permanent magnet linear motor for power conversion, it can reduce the loss of the transmission device during the energy transfer process. The output power of the double blunt body vortex-induced vibration generation system is 1.53 times higher than that of the single blunt body structure, and the energy conversion efficiency is increased by 12.33%.

In summary, the technology proposed in this paper is of great significance for the efficient use of low-flow current energy. Vortex-induced vibration power generation technology has great potential for marine and riverine energy utilization. In deep-sea environments, where water velocities are typically low, the technology can be utilized to provide energy for deep-sea exploration equipment or undersea sensor networks. In addition, it could be used as an auxiliary power source for ships; ships could be equipped with vortex-induced vibration power generation systems that utilize the kinetic energy of water currents during navigation to generate auxiliary power. This additional power can support various shipboard systems, such as navigation instruments, communications equipment, and scientific research tools. Through further research and optimization, this vortex-induced vibration generation system can be used under conditions where traditional turbine generators cannot work. This vortex-induced vibration generation system can complement the advantages of traditional turbine generation and is expected to be an effective tool for ocean energy development.

Author Contributions: Conceptualization and methodology, G.L.; methodology, writing—review and editing, H.X.; software, validation and writing—original draft preparation, L.F.; supervision, X.S.; data curation, C.X.; investigation, J.W. All authors have read and agreed to the published version of the manuscript.

Funding: This research was funded by the Beijing Natural Science Foundation Joint Fund (L244011) and Chinese Academy of Sciences Strategic Pilot Science and Technology Program (Category A), (XDA22010401).

Data Availability Statement: The data that support the findings of this study are available on request from the corresponding author.

Conflicts of Interest: The authors declare no conflicts of interest.

Appendix A.

Appendix A.1. Mathematical Model of Vortex Excitation Vibration

According to the equivalent spring–mass–damping system, the differential equation of motion for vortex-induced vibration can be obtained:

$$M_0\ddot{y} + C_0\dot{y} + K_0 y = F(t) \tag{A1}$$

where $\ddot{y}$, $\dot{y}$, y are the acceleration, velocity, and displacement of the vibrating system, respectively, M_0 is the total mass of the vibrating system, C_0 is the damping of the system, and K_0 is the stiffness of the system. During the motion, the vibrator is subjected to the vortex excitation force $F(t)$ from the water flow in addition to the inertia, damping, and stiffness forces.

Considering that the elastomer is connected to the oscillator and that the oscillator moves a portion of the fluid when it vibrates, the vibrating mass is really the sum of the mass of the blunt body m_b, the mass of the fluid m_f, and 1/3 of the mass of the spring m_{spr}:

$$M_0 = m_b + m_f + \frac{1}{3}m_{spr} \tag{A2}$$

The mass of the additional fluid is calculated using an empirical formula, which is closely related to the volume of the blunt body. Where C_M is the additional mass coefficient usually selected, $C_M = 1$. D_b is the diameter of the blunt body, L_b is the characteristic length of the blunt body, and ρ_f is the fluid density.

$$m_f = \frac{\pi}{4}C_{M}\rho_f D_b^2 L_b \tag{A3}$$

Similarly, damping consists of two items, mechanical damping C_s and fluid damping C_f:

$$C_0 = C_s + C_f \tag{A4}$$

$$C_f = \gamma\omega_f\rho_f D_b^2 \tag{A5}$$

$$\omega_f = 2\pi U_{fluid}St/D_b \tag{A6}$$

where γ is a constant, ω_f is the angular frequency of vortex shedding, St is the Strauhl number, and U_{fluid} is the fluid flow rate. The stiffness K_0 of the vibrating system is related to the angular frequency ω_S of the blunt body and the mass M_0, expressed as follows:

$$K_0 = M_0 + \omega_s^2 \tag{A7}$$

Referring to the existing findings on vortex excitation, it is found to be related to parameters such as the size of the blunt body, the density of the fluid, the incoming flow velocity, etc., and is expressed as follows:

$$F = \frac{\rho {U_{fluid}}^2 D_b L_b}{2}\cdot\frac{C_L}{2}\cdot q - \frac{\rho_f U_{fluid} D_b L_b}{2}C_D\dot{y} \tag{A8}$$

where C_L is the lift coefficient and C_D is the drag coefficient. The lift coefficient and drag coefficient are dimensionless forms of lift and drag, which are dimensionless according to the area and expressed as follows:

$$C_L = \frac{2F_L}{\rho_f {U_{fluid}}^2 E_0} \tag{A9}$$

$$C_D = \frac{2F_D}{\rho_f {U_{fluid}}^2 E_0} \tag{A10}$$

where F_L and F_D are the lift and drag forces, respectively, and E_0 is the projected area.

Regarding the vibration of the wake oscillator due to vortex shedding, it can be expressed in terms of the van der Pol equation by adding the mechanical coupling force to the equation, denoted as follows:

$$\ddot{q} + \varepsilon w_f\left(q^2 - 1\right)\dot{q} + w_f^2 q = Q\ddot{y} \tag{A11}$$

where ε and Q are experimental constants. The van der Pol equation is a nonlinear second-order differential equation that can be solved in a reduced order manner.

Let $\xi = C_s/2m\omega_s$ and $\mu = m/\rho_f D_b^2$, and then the mathematical model of vortex-induced vibration combining fluid and solid can be simplified as follows:

$$\begin{cases} M_0\ddot{y} + M_0\left(2\xi\omega_s + \frac{\gamma}{\mu}w_f\right)\dot{y} + M_0\omega_s^2 y = \frac{\rho_f {U_{fluid}}^2 D_b L_b}{2}\cdot\frac{C_L}{2}\cdot q - \frac{\rho_f U_{fluid} D_b L_b}{2}C_D\dot{y} \\ \ddot{q} + \varepsilon w_f\left(q^2-1\right)\dot{q} + w_f^2 q = Q\ddot{y} \end{cases} \tag{A12}$$

where q is the tailing vibration displacement, $\dot{q}$ is the tailing vibration velocity, and $\ddot{q}$ is the tailing vibration acceleration. From Equation (A12), It can be seen that the vortex-induced vibration mathematical model is a second-order nonlinear differential equation with fluid–solid coupling, which can be solved by means of reduced order.

Appendix A.2. Center Finite Difference Method for Solving Vortex-Induced Vibration Response Equations

First, the problem of solving a system of differential equations is transformed into a problem of solving a system of algebraic equations by expressing the first-order differential vectors and the second-order differential vectors in the vibration equations in terms of combinations of displacements. Then, the recursive formulas for each differential interval are found in the time interval, which in turn leads to the response of the whole time scale. The finite center differential method satisfies the equations of motion only for discrete time intervals separated by a period of time Δt. Using equal time steps, the expression for the $\ddot{y}, \dot{y}, \ddot{q}, \dot{q}$ discretization is obtained:

$$\dot{y} = \frac{y_{i+1} - y_{i-1}}{2\Delta t},\ \ddot{y} = \frac{y_{i+1} - 2y_i + y_{i-1}}{\Delta t^2} \tag{A13}$$

$$\dot{q} = \frac{q_{i+1} - q_{i-1}}{2\Delta t},\ \ddot{q} = \frac{q_{i+1} - 2q_i + q_{i-1}}{\Delta t^2} \tag{A14}$$

The discrete first-order and second-order terms are brought into the system of coupled vibration equations and organized to obtain the equations of the latter moment with the previous two moments. According to the discrete set of vibration equations, the initial conditions are determined, and the displacements and velocities at the zero moment are set to be $\dot{y}_0 = 0, y_0 = 0, \dot{q}_0 = 0, q_0 = 0, V_0 = 0$. The second-order term at the zero moment is obtained according to the equations of motion at the zero moment. The system is given a small initial excitation force as the initial value of the second-order term is zero when the flow rate is a steady value, and then no vibration occurs. The displacement before the zero moment is expressed by y_{-1} and q_{-1}. According to the above two equations, the first- and second-order functions at the zero moment can be obtained:

$$\left(\frac{M_0}{\Delta t^2} + \frac{C}{2\Delta t}\right)y_i = \left(\frac{2M_0}{\Delta t^2} - M_0\omega_s^2\right)y_{i-1} + \left(\frac{C}{2\Delta t} - \frac{M_0}{\Delta t^2}\right)y_{i-2} + \frac{\rho_f {U_{fluid}}^2 D_b L_b}{2}\cdot\frac{C_L}{2}q_{i-1} \tag{A15}$$

$$\left(\frac{1}{\Delta t^2} + \frac{\varepsilon w_f\left({q_{i-1}}^2 - 1\right)}{2\Delta t}\right)q_i = \left(\frac{2}{\Delta t^2} - w_f^2\right)q_{i-1} + \left(\frac{\varepsilon w_f\left({q_{i-1}}^2 - 1\right)}{2\Delta t} - \frac{1}{\Delta t^2}\right)q_{i-2} + \frac{Q}{D_b}\ddot{y}_{i-1} \tag{A16}$$

$$C = M_0\left(2\xi\omega_s + \frac{\gamma}{\mu}w_f\right) + \frac{\rho_f U_{fluid} D_b L_b C_D}{2} \tag{A17}$$

Since y_{-1} and q_{-1} are solved in the same way, the generalized solution is denoted by u_{-1}, that is

$$\dot{u}_0 = \frac{u_{1-}u_{-1}}{2\Delta t} \tag{A18}$$

$$\ddot{u}_0 = \frac{u_1 - 2u_0 + u_{-1}}{\Delta t^2} \tag{A19}$$

The above two equations are obtained by eliminating u_1:

$$u_{-1} = u_0 - \Delta t \dot{u}_0 + \frac{\Delta t^2}{2} \ddot{u}_0 \tag{A20}$$

Given the solution time step and total solution time, the number of iterations is calculated and the solution is completed. The above are the steps of solving the mathematical model of vortex-induced vibration using the central finite difference method. The model has second-order accuracy, the error satisfies $\varepsilon \propto O\left(\Delta T^2\right)$, and the stability condition is $\Delta t \leq T_n/\pi$, where T_n is the self-oscillation period of the oscillator. For the multi-degree-of-freedom system, T_n is the minimum self-oscillation period of the structure, $T_n = 2\pi/\omega$.

References

1. Magagna, D.; Uihlein, A. Ocean energy development in Europe: Current status and future perspectives. *Int. J. Mar. Energy* **2015**, *11*, 84–104. [CrossRef]
2. Zhang, K.-M.; Wen, Z.-G. Review and challenges of policies of environmental protection and sustainable development in China. *J. Environ. Manag.* **2008**, *88*, 1249–1261. [CrossRef] [PubMed]
3. Khan, N.D.; Kalair, A.; Abas, N.; Haider, A. Review of ocean tidal, wave and thermal energy technologies. *Renew. Sustain. Energy Rev.* **2017**, *72*, 590–604. [CrossRef]
4. Rostami, A.B.; Armandei, M. Renewable energy harvesting by vortex-induced motions: Review and benchmarking of technologies. *Renew. Sustain. Energy Rev.* **2017**, *70*, 193–214. [CrossRef]
5. Ding, L.; Zhang, L.; Wu, C.; Mao, X.; Jiang, D. Flow induced motion and energy harvesting of bluff bodies with different cross sections. *Energy Convers. Manag.* **2015**, *91*, 416–426. [CrossRef]
6. Khalak, A.; Williamson, C.H.K. Fluid Forces and Dynamics of a Hydroelastic Structure with Very Low Mass and Damping. *J. Fluids Struct.* **1997**, *11*, 973–982. [CrossRef]
7. Bernitsas, M.M.; Ben-Simon, Y.; Raghavan, K.; Garcia, E. The VIVACE converter: Model tests at high damping and Reynolds number around 105. In Proceedings of the International Conference on Offshore Mechanics and Arctic Engineering, Hamburg, Germany, 4–9 June 2006.
8. Bernitsas, M.M.; Raghavan, K.; Ben-Simon, Y.; Garcia, E.M.H. VIVACE (Vortex Induced Vibration Aquatic Clean Energy): A new concept in generation of clean and renewable energy from fluid flow. *J. Offshore Mech. Arct. Eng.* **2008**, *130*, 041101. [CrossRef]
9. Bernitsas, M.M.; Raghavan, K.; Duchene, G. Induced separation and vorticity using roughness in VIV of circular cylinders at $8 \times 103 < \mathrm{Re} < 2.0 \times 105$. In Proceedings of the International Conference on Offshore Mechanics and Arctic Engineering, Estoril, Portugal, 5–20 June 2008.
10. Li, H.; Bernitsas, C.C.; Congpuong, N.; Bernitsas, M.M.; Sun, H. Experimental investigation on synergistic flow-induced oscillation of three rough tandem-cylinders in hydrokinetic energy conversion. *Appl. Energy* **2024**, *359*, 122587. [CrossRef]
11. Zhou, S.; Wang, J. Dual serial vortex-induced energy harvesting system for enhanced energy harvesting. *AIP Adv.* **2018**, *8*, 075221. [CrossRef]
12. Hamdan, C.; Allport, J.; Sajedin, A. Piezoelectric power generation from the vortex-induced vibrations of a semi-cylinder exposed to water flow. *Energies* **2021**, *14*, 6964. [CrossRef]
13. Luo, Y.; Wu, H.; Huang, S.; Sun, H. Energy Harnessing Performance of Oscillating Foil Submerged in the Wake of a Fixed Cylinder. *Energies* **2024**, *17*, 1793. [CrossRef]
14. Park, H.; Mentzelopoulos, A.P.; Bernitsas, M.M. Hydrokinetic energy harvesting from slow currents using flow-induced oscillations. *Renew. Energy* **2023**, *214*, 242–254. [CrossRef]
15. Zhang, B.; Li, B.; Fu, S.; Ding, W.; Mao, Z. Experimental investigation of the effect of high damping on the VIV energy converter near the free surface. *Energy* **2022**, *244*, 122677. [CrossRef]
16. Wang, J.; Xia, B.; Yurchenko, D.; Litak, G.; Li, Y.; Tian, H. Enhanced performance of piezoelectric energy harvester by two asymmetrical splitter plates. *Ocean Eng.* **2023**, *270*, 113614. [CrossRef]
17. Li, X.; Zhou, Y.; Li, Z.; Guo, H.; Gong, Y.; Zhang, D.; Zhang, D.; Zhang, Q.; Wang, B.; Peng, Y. Vortex-induced vibration triboelectric nanogenerator for energy harvesting from low-frequency water flow. *Energy Convers. Manag.* **2023**, *292*, 117383. [CrossRef]
18. Heragy, M.; Kiwata, T.; Hamano, T.; Shima, T.; Ueno, T.; Kono, T.; Ekmekci, A. Experimental study of wind energy harvesting from flow-induced vibration of prisms using magnetostrictive material. *J. Fluids Struct.* **2023**, *119*, 103910. [CrossRef]
19. Guo, X.; Yang, M.; Li, F.; Zhu, Z.; Cui, B. Investigation on Cryogenic Cavitation Characteristics of an Inducer Considering Thermodynamic Effects. *Energies* **2024**, *17*, 3627. [CrossRef]
20. Wu, J.; Xu, P.; Li, L.; Li, Z.; Qi, H.; Wang, C.; Zhang, Y.; Xie, Y.; Tan, D. Multiphase dynamic interfaces and abrasive transport dynamics for abrasive flow machining in shear thickening transition states. *Powder Technol.* **2024**, *446*, 120150. [CrossRef]
21. Xue, B.; Wang, S.-P.; Peng, Y.-X.; Zhang, A.-M. A novel coupled Riemann SPH–RKPM model for the simulation of weakly compressible fluid–structure interaction problems. *Ocean Eng.* **2022**, *266*, 112447. [CrossRef]

22. Ge, M.; Zheng, G. Fluid–Solid Mixing Transfer Mechanism and Flow Patterns of the Double-Layered Impeller Stirring Tank by the CFD-DEM Method. *Energies* **2024**, *17*, 1513. [CrossRef]
23. Sarout, Y.; Islam; Fatt, Y.; Janajreh, I. Flow around an oscillating cylinder at low Reynolds number with forced convection: Effect of corner radius and Reynolds number. *Energies* **2022**, *15*, 9145. [CrossRef]
24. Qiu, T.; Xu, Q.; Du, X.; Zhao, Y.; Lin, W. VIV of twin square cylinders in various configurations at a low Reynolds number. *Ocean Eng.* **2022**, *260*, 112067. [CrossRef]
25. Lian, J.; Wu, Z.; Yao, S.; Yan, X.; Wang, X.; Jia, Z.; Long, Y.; Shao, N.; Yang, D.; Li, X. Experimental investigation of flow-Induced motion and energy conversion for two rigidly coupled triangular prisms arranged in tandem. *Energies* **2022**, *15*, 8190. [CrossRef]
26. Chen, W.; Ji, C.; Xu, D.; An, H.; Zhang, Z. Flow-induced vibrations of two side-by-side circular cylinders at low Reynolds numbers. *Phys. Fluids* **2020**, *32*, 244–257. [CrossRef]

Disclaimer/Publisher's Note: The statements, opinions and data contained in all publications are solely those of the individual author(s) and contributor(s) and not of MDPI and/or the editor(s). MDPI and/or the editor(s) disclaim responsibility for any injury to people or property resulting from any ideas, methods, instructions or products referred to in the content.